Efficient targeted energy transfer of bistable nonlinear energy sink: application to optimal design

Donghai Qiu, Tao Li, Sébastien Seguy, Manuel Paredes

Noname manuscript No.
(will be inserted by the editor)

Efficient targeted energy transfer of bistable nonlinear energy sink: application to optimal design

Donghai Qiu · Tao Li · Sébastien Seguy · Manuel Paredes

Received: date / Accepted: date

Abstract This paper is dedicated to the optimal design of a bistable nonlinear energy sink (NES) for the vibration control of a periodically excited linear oscillator. This system with negative linear and cubic nonlinear coupling is analytically studied with the method of multiple scales. As a result, a slow invariant manifold (SIM) is obtained and is applied to predict four typical response regimes at different energy levels. Moreover, asymptotic analysis and Melnikov analysis are respectively used to obtain the thresholds of these typical responses. Through their efficiency comparison, it is observed that the bistable NES can be efficient and robust in a broad-range of excitation amplitude. With the Hilbert transform and wavelet transform, Targeted energy transfer (TET) with transient or permanent 1:1 resonance is found to be responsible for the effectiveness of such responses as strongly modulated response and 1:1 resonance. Finally, an optimal design criterion and a corresponding parameter configuration are proposed to guide the application of this type of NES.

Keywords Targeted energy transfer · Bistable NES · Slow invariant manifold · Strongly modulated response · Excitation threshold · Optimal design

D. Qiu · T. Li · S. Seguy · M. Paredes
Institut Clément Ader (ICA), CNRS-INSA-ISAE-Mines Albi-UPS, Université de Toulouse, 3 rue Caroline Aigle, F-31077 31400, Toulouse, France
E-mail: qiu@insa-toulouse.fr

Tao Li
E-mail: tli@insa-toulouse.fr

Sébastien Seguy
E-mail: sebastien.seguy@insa-toulouse.fr

Manuel Paredes
E-mail: manuel.paredes@insa-toulouse.fr

1 Introduction

Mitigation of unwanted vibration is an important issue in many fields of engineering. Since the emergence of innovative absorber Nonlinear Energy Sink (NES), more attentions are paid to this promising technique [1,2]. This type of absorber is characterized by a secondary mass strongly coupled with a nonlinear stiffness to the main structure that needs to be protected. By triggering resonances between related nonlinear normal modes, the nonlinearity allows energy to be irreversibly transfered from the main structure to the secondary mass [3,4]. Unlike the traditional linear absorber, the Tuned Mass Damper (TMD), which needs to be tuned to a specific natural frequency, NES can passively absorb energy over a wide range of natural frequencies [5]. In addition, its relatively small mass, makes it particularly attractive in a wide variety of applications such as space and aero-structures [6], vibrating machinery [7, 8], buildings [9,10] and vehicle suspensions [11].

The design of the nonlinearity is a key element to obtain optimum performance of NES. Depending on the type of nonlinearity, various kinds of NES have been proposed and studied, such as oscillating dissipative attachments with essentially strong cubic stiffness [12, 13], rotational element [14,15], piece-wise NES [16,17], vibro-impact NES [18,19], NES by nonlinear membrane [20] and magnet based NES [21]. Substantial theoretical experimental work has been achieved to verify the performance of NES under transient and periodic excitation [22–27]. In these works, the topological structure of Slow Invariant Manifold (SIM) is commonly used to predict the response of NES. In this structure, the unstable branch corresponds well to the strongly modulated response (SMR) which exhibits more efficient performance than the other steady-state response [27].

However, the energy threshold corresponding to SMR is normally narrow, making the NES sensitive to the excitation amplitude and thus restricting its use in engineering applications.

Recent works seeking to improve the robustness of excitation have observed that the bistable NES shows significant advantages with respect to energy pumping efficiency [28–34]. This NES, with negative stiffness and nonlinear stiffness components, has nonzero displacement relative to the linear oscillator (LO) away from the NES equilibrium positions [32]. This leads to strong suppression of the vibration amplitude of the LO in the first cycle of oscillation for a wide range of initial input energies induced in the linear structure. The analytical and numerical aspects of the transient dynamics of bistable NES are explored in [35] and [36], respectively. With the Limiting Phase Trajectories (LPTs) and Poincare section, dynamic mechanisms depending on different types of impulse input are proposed: for high energy levels, strongly modulated oscillation occurs and the dynamics are governed by fundamental (1:1) and superharmonic (1:3) resonances; for low energy levels, chaotic cross-well oscillations of the nonlinear attachment together with subharmonic resonances lead to strong energy exchanges between the two oscillators. In [37], Lyapunov characteristic exponents and Melnikov analysis are adopted to identify the region where chaotic cross-well oscillations exist as low-intensity impulse applied to the LO. The experimental aspect of a system consisting of a Bernouli-Euler beam coupled to a continuous bistable NES is developed in [38] and shows that this NES can achieve efficient TET under a wide-range of impacts. In [39], a system of two coupled cantilever beams coupled to a bistable light attachment is tested and proves that this NES has better efficiency in frequency than existing passive devices.

From these researches, it reveals that an appropriately designed bistable NES can be more efficient than the NES types enumerated above. However, recent studies have mainly focused on the transient dynamics between a conservative system with impulsively excited LO and a NES. The efficiency of each response regime and its corresponding threshold under periodic excitation are uncertain, so the optimal design criterion of bistable NES needs to be further studied. With this in mind, the main objective of the work presented here is first to study the efficiency of different response regimes and then to establish the relation of optimization for different excitation conditions.

In this paper, a 2 DOF system comprising a harmonically excited LO strongly coupled to a bistable NES is investigated theoretically. In Sec. 2, the equation of motion is studied analytically with the method of multiple scales. The response regimes and the transient trajectory projected in the SIM are observed. Then asymptotic analysis and Melnikov analysis are respectively used to obtain the thresholds at different energy levels. In Sec. 3, the efficiency of different response regimes is compared and their underlying TET is presented. An optimal design criterion of bistable NES is proposed. Finally, the conclusion is addressed.

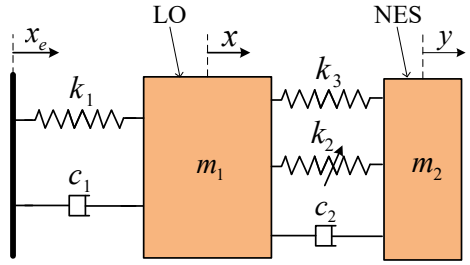

Fig. 1 Schematic of the 2 DOF system comprising a LO and a bistable NES

2 Theoretical Development

2.1 Modelling and analytical treatment

The system of a harmonically excited linear oscillator (LO) with a bistable NES is illustrated in Fig. 1, and the equations of motion are as follows:

$$\begin{cases} m_1\ddot{x} + k_1 x + c_1\dot{x} + c_2\left(\dot{x}-\dot{y}\right) + k_2\left(x-y\right)^3 \\ +k_3(x-y) = k_1 x_e + c_1\dot{x}_e \\ m_2\ddot{y} + c_2(\dot{y}-\dot{x}) + k_2\left(y-x\right)^3 + k_3(y-x) = 0 \end{cases} \tag{1}$$

where x, m_1, c_1, k_1 and y, m_2, c_2, k_2, k_3 are the displacement, mass, damping and stiffness of the LO and the bistable NES respectively, the dots denote differentiation with respect to time. The imposed harmonic displacement $x_e$is expressed as follows:

$$x_e = Gcos(\omega t) \tag{2}$$

After rescaling, the system of equation (1) can be reduced to the dimensionless form:

$$\begin{cases} \ddot{x} + x + \epsilon\lambda_1\dot{x} + \epsilon\lambda_2\left(\dot{x}-\dot{y}\right) + \epsilon K\left(x-y\right)^3 + \epsilon\delta(x-y) \\ = \epsilon F\cos\Omega\tau \\ \epsilon\ddot{y} + \epsilon\lambda_2\left(\dot{y}-\dot{x}\right) + \epsilon K\left(y-x\right)^3 + \epsilon\delta(y-x) = 0 \end{cases} \tag{3}$$

where the term containing ϵ^2 is small and can be neglected. The corresponding physical parameters are expressed as follows:

$$\begin{gathered}\epsilon=\frac{m_2}{m_1},\quad {\omega_0}^2=\frac{k_1}{m_1},\quad K=\frac{k_2}{m_2{\omega_0}^2},\\ \delta=\frac{k_3}{m_2{\omega_0}^2},\quad \lambda_1=\frac{c_1}{m_2\omega_0},\quad \lambda_2=\frac{c_2}{m_2\omega_0},\\ F=\frac{G}{\epsilon},\quad \Omega=\frac{\omega}{\omega_0},\quad \tau=\omega_0 t\end{gathered} \tag{4}$$

New variables representing the displacement of the centre of mass and the internal displacement of the bistable NES are introduced:

$$v=x+\epsilon y,\quad w=x-y \tag{5}$$

Substituting Eqs. (5) into Eqs. (3):

$$\begin{cases}\ddot{v}+\epsilon\lambda_1\dfrac{\dot{v}+\epsilon\dot{w}}{1+\epsilon}+\dfrac{v+\epsilon w}{1+\epsilon}=\epsilon F\cos\Omega\tau\\ \ddot{w}+\epsilon\lambda_1\dfrac{\dot{v}+\epsilon\dot{w}}{1+\epsilon}+\dfrac{v+\epsilon w}{1+\epsilon}+\lambda_2\left(1+\epsilon\right)\dot{w}\\ +K\left(1+\epsilon\right)w^3+\delta(1+\epsilon)w=\epsilon F\cos\Omega t\end{cases} \tag{6}$$

The system is studied in the vicinity of the 1:1 resonance, where both the LO and the NES execute time-periodic oscillations with identical frequency Ω. To obtain the analytical periodic solution, two new complex variables are introduced:

$$\phi_1 e^{i\Omega\tau}=\dot{v}+i\Omega v,\quad \phi_2 e^{i\Omega\tau}=\dot{w}+i\Omega w \tag{7}$$

Substituting Eqs. (7) into Eqs. (6) and keeping only the secular term containing $e^{i\Omega\tau}$ yields the following slowly modulated system:

$$\begin{cases}\dot{\phi}_1+\frac{i\Omega}{2}\phi_1+\frac{\epsilon\lambda_1(\phi_1+\epsilon\phi_2)}{2(1+\epsilon)}-\frac{i(\phi_1+\epsilon\phi_2)}{2\Omega(1+\epsilon)}-\frac{\epsilon F}{2}=0\\ \dot{\phi}_2+\frac{i\Omega}{2}\phi_2+\frac{\epsilon\lambda_1(\phi_1+\epsilon\phi_2)}{2(1+\epsilon)}-\frac{i(\phi_1+\varepsilon\phi_2)}{2\Omega(1+\epsilon)}+\frac{\lambda_2(1+\epsilon)\phi_2}{2}\\ -\frac{3iK(1+\epsilon)\phi_2^2\bar{\phi}_2}{8\Omega^3}-\frac{\epsilon F}{2}-\frac{i\phi_2\delta(1+\epsilon)}{2\Omega}=0\end{cases} \tag{8}$$

A detuning parameter σ representing the nearness of the excitation frequency ω to the reduced natural frequency of the LO is introduced:

$$\Omega=1+\epsilon\sigma \tag{9}$$

In the context of energy pumping, the mass ratio ϵ is taken to be small ($\approx 1\%$). In this case, Eq. (8) may be analysed by a perturbation method with respect to this small parameter. For this purpose, the method of multiple scales is introduced in the following form:

$$\begin{gathered}\phi_i=\phi_i(\tau_0,\tau_1,\ldots),\quad \frac{d}{d\tau}=\frac{\partial}{\partial\tau_0}+\epsilon\frac{\partial}{\partial\tau_1}+\ldots\\ \tau_k=\epsilon^k\tau,\quad k=0,1,\ldots\end{gathered} \tag{10}$$

Substituting Eq. (9) and Eqs. (10) into Eqs. (8) and equating coefficients of ϵ^0 and ϵ^1 gives:

Order ϵ^0:

$$\begin{cases}\frac{d}{d\tau_0}\phi_1=0\\ \frac{d}{d\tau_0}\phi_2+\frac{1}{2}i(\phi_2-\phi_1)+\frac{1}{2}\phi_2\lambda_2\\ -\frac{3}{8}iK{\phi_2}^2\bar{\phi}_2-\frac{1}{2}i\delta\,\phi_2=0\end{cases} \tag{11}$$

Order ϵ^1:

$$\begin{cases}\frac{d}{d\tau_1}\phi_1+\frac{1}{2}\lambda_1\phi_1+\frac{1}{2}i\left(\phi_1-\phi_2\right)+i\sigma\,\phi_1-\frac{1}{2}F=0\\ \frac{d}{d\tau_1}\phi_2+\frac{1}{2}\lambda_1\phi_1+\frac{1}{2}\phi_2\lambda_2+\frac{1}{2}i\sigma\,\left(\phi_1+\phi_2\right)\\ +\frac{1}{2}i\left(\phi_1-\phi_2\right)-\frac{3}{8}iK\left(1-3\,\sigma\right)\phi_2{}^2\bar{\phi}_2-\frac{1}{2}F\\ +\frac{1}{2}i\delta\,\left(\sigma-1\right)\phi_2=0\end{cases} \tag{12}$$

Then we introduce the new variables:

$$\phi_1(\tau_1)=N_1e^{i\theta_1},\quad \phi_2(\tau_1)=N_2e^{i\theta_2} \tag{13}$$

where N_1, N_2 and θ_1, θ_2 respectively represent the amplitude and phase angle of the LO and NES. With this change of variables in Eqs. (11), the expression for a slow invariant manifold (SIM) is obtained:

$$\begin{gathered}Z_1=\lambda_2^2Z_2+(\delta-1)^2Z_2+\frac{3K}{2}(\delta-1){Z_2}^2+\frac{9K^2}{16}{Z_2}^3\\ Z_1={N_1}^2,\quad Z_2={N_2}^2\end{gathered} \tag{14}$$

By taking the derivative of the right-hand side with respect to Z_2, the multiplicity of solutions can be studied. After resolution, the singular values of Z_2 are calculated:

$$Z_{2i}=\frac{4\left(2(1-\delta)\pm\sqrt{(1-\delta)^2-3\lambda_2^2}\right)}{9K} \tag{15}$$

In Eq. (15), the existence of two roots and a pair of saddle-node bifurcations needs to satisfy the condition:

$$\delta<1-\sqrt{3}\lambda_2 \tag{16}$$

If δ is greater than this critical value, the SIM is monotonous. Otherwise, the SIM admits extrema and

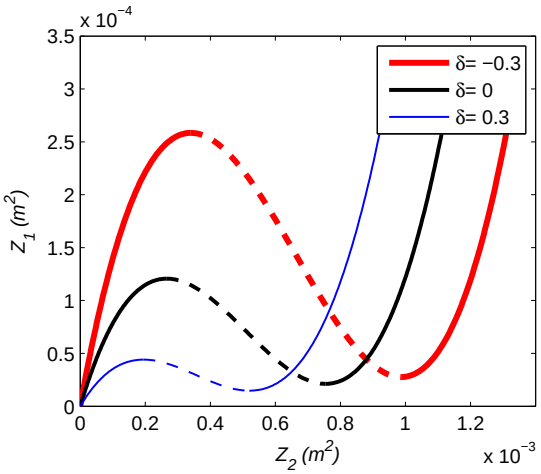

Fig. 2 The SIM structure with different value of δ. The solid line represents the stable branch, and the dotted line the unstable branch

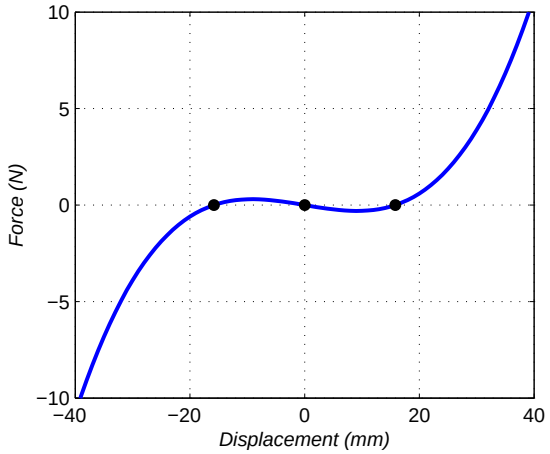

Fig. 3 The force displacement relation of a bistable NES: the two side points represent the two stable equilibria, and the middle point represents the unstable equilibrium

can be divided into two stable branches and one unstable branch.

An illustration of a SIM with different values of δ is given in Fig. 2. When the value of δ decreases, the topological shape of the SIM becomes larger and the unstable branch is shifted towards the right up direction. For a cubic NES as $\delta = 0$, the unstable branch of SIM is mainly responsible for the possible occurrence of energy pumping and it may give rise to the strongly modulated response (SMR)[26]. For a bistable NES as $\delta < 0$, the relation between the unstable branch and the SMR is uncertain. So in the next section, the response regimes and the corresponding SIM positions will be discussed.

2.2 Response regimes

The parameters identified on the simulation setup and used for the calculations are given in Tab. 1. The corresponding force-displacement relation of a bistable NES is presented in Fig. 3, where the curve has two stable equilibria and an unstable equilibrium. The region of negative stiffness is located between the two stable equilibrium points. In this area, the dynamic transition is rapid and sweeps out a large stroke, thus including viscous damping that can provide high levels of energy dissipation. If these parameters are transferred to the double-well restoring force potential, four different response regimes are obtained, as shown in Fig. 4, which illustrates that, with different levels of input energy, the dynamic response of a bistable NES can be classified as (a) intra-well oscillation, (b) chaotic inter-well oscillation, (c) strongly modulated response and (d) stable periodic response.

Table 1 Parameters of bistable NES

Physical Parameters			
m_1	$5\,kg$	k_1	$11.4 \times 10^3\ N/m$
m_2	$50\,g$	k_2	$2 \times 10^5\ N/m^3$
c_1	$4\,Ns/m$	k_3	$-50\ N/m$
c_2	$0.4\,Ns/m$		
Reduced Parameters			
ϵ	1%	λ_1	1.67
K	1742	λ_2	0.167
δ	−0.44		

To demonstrate these regimes, the time-displacement response of the LO and NES, and the projection of motion of the system into SIM are presented in Fig. 5, in the first and second column, respectively. Where the simulation model is described by Fig. 1 under periodic excitation, the transient modulus of the LO and NES are calculated by $Z_1 = \left|(\dot{v} + i\Omega v)e^{-i\Omega\tau}\right|^2$ and $Z_2 = \left|(\dot{w} + i\Omega w)e^{-i\Omega\tau}\right|^2$. As a result, the following response regimes will occur consecutively with increasing excitation amplitude:

(a) Intra-well oscillation with $G = 0.06\ mm$. In this case, the NES exhibits a small amplitude response of oscillation about one of the stable equilibria (the dashed line). Owing to the asymmetric of amplitude of the NES, the projection in the SIM structure is a cyclic motion around the stable equilibrium, and the location is far away from the first stable branch of the SIM;

(b) As the excitation amplitude G increases to 0.1 mm, chaotic alternating in-well and cross-well oscillations are observed, the two stable equilibria of which are

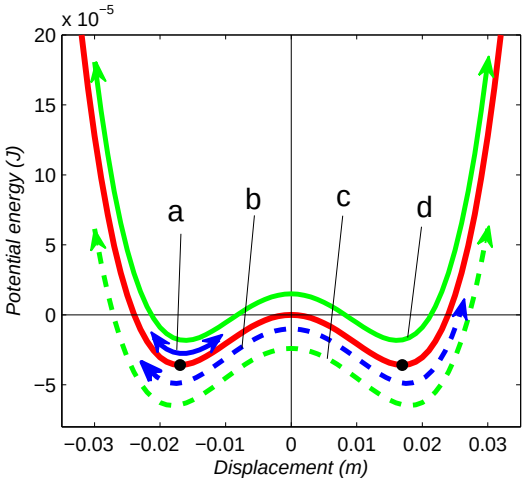

Fig. 4 Responses at different levels of energy: ***a*** intra-well oscillation; ***b*** chaotic inter-well oscillation; ***c*** strongly modulated response; ***d*** stable periodic response

indicated by two horizontal dashed lines in the time response plots and by the vertical dashed line in the SIM plots. Taking the dashed line as a reference, it illustrates that the amplitude of cross-well oscillations is close to the value of stable equilibrium. With the characteristics of irregular in both duration and occurrence, the transient trajectory in SIM is chaotic and not repeatable;

(c) For a relatively higher level of excitation amplitude $G = 0.42\ mm$, a quasi-periodic regime with slow variation of the amplitudes of both oscillators is observed. For the LO, the amplitude increases and decreases repeatedly in a regular fashion. The amplitude of the bistable NES can be roughly classified into two regimes: a small region (chaotic and growing envelope) corresponding to the increase of the LO amplitude, and a large region (relatively stable envelope) corresponding to the decrease of the LO amplitude. This alternating regime of strongly modulated response (SMR) produces the jump phenomenon in SIM. However, unlike the cubic NES, the hypothetical jump of bistable NES does not start from the first singular point, which means that the first stable branch of SIM can not predict the threshold of targeted energy transfer;

(d) As the excitation amplitude is increased still further to $G = 0.55\ mm$, both the LO and NES show a stable periodic response, the amplitudes of which are symmetrical. This means that 1:1 resonance of LO and NES is produced. The corresponding right sub-figure shows that the steady projected motion focuses on the second stable branch of the SIM, and it has been demonstrated in [27] that this projection can be represented by a fixed point of the SIM.

Knowing the variation mechanism of the response regimes, it would be interesting to investigate the efficiency of each regime and the corresponding threshold for periodic excitation so as to guide the design of a bistable NES. When the input energy is high, as shown in Fig. 4, there is a threshold that fixes whether SMR (c) or the stable periodic response (d) is obtained. By comparing the two SIM projections of Fig. 5, a critical fixed point located at the lowest point of the second stable branch can be found, and its position can be used to evaluate the type of response regime. For the low level of energy, the state of the bistable NES can be imagined as a ball moving in the 'double-well' structure, the dynamic response of which is restricted to oscillations confined to one stable state corresponding to response (a). When sufficient energy is input to elevate the state beyond the hilltop, the second response (b) alternating in-well and cross-well oscillation is produced. In physical terms, this hilltop analogy can be defined as a force threshold or critical load. Based on the above analysis, the threshold and the efficiency of each regime will be studied further in the following sections.

3 Study of threshold at different levels of energy

3.1 Asymptotic analysis for high energy level

To obtain the threshold at high energy level, asymptotic analysis will continue to be used so as to analyse the bifurcations of the SMR regime. The fixed point corresponding to periodic responses is described in Eqs. (11), and we assume the solution on the stable branch to be $\Phi(\tau_1) = \lim_{\tau_0 \to \infty} \phi_2(\tau_0, \tau_1)$. By introducing this expression and Eqs. (11) into the first equation of Eqs. (12), the asymptotic stability of the points of the stable branch with respect to time scale τ_1 is studied in the following form:

$$\begin{aligned} &\tfrac{d}{d\tau_1}\Phi(1 - i\lambda_2 - \delta - \tfrac{3}{2}K\Phi\bar{\Phi}) - \tfrac{d}{d\tau_1}\bar{\Phi}\tfrac{3}{4}K\Phi^2 \\ &-\tfrac{3}{8}iK\Phi^2\bar{\Phi}(1 - i\lambda_1 + 2\sigma) + \tfrac{1}{2}\Phi(2i\sigma + \lambda_1 + \lambda_2 \\ &-\sigma\lambda_1 - i\delta + 2\sigma\lambda_2 - 2i\sigma\delta - i\lambda_1\lambda_2) - \tfrac{1}{2}F = 0 \end{aligned} \tag{17}$$

By transferring $\Phi(\tau_1)$ into polar coordinates, the expression governing the evolution of amplitude N_2 and the phase angle θ_2 are obtained:

$$\frac{\partial N_2}{\partial \tau_1} = \frac{f_2(N_2, \theta_2)}{g(N_2)}, \quad \frac{\partial \theta_2}{\partial \tau_1} = \frac{f_1(N_2, \theta_2)}{g(N_2)} \tag{18}$$

where

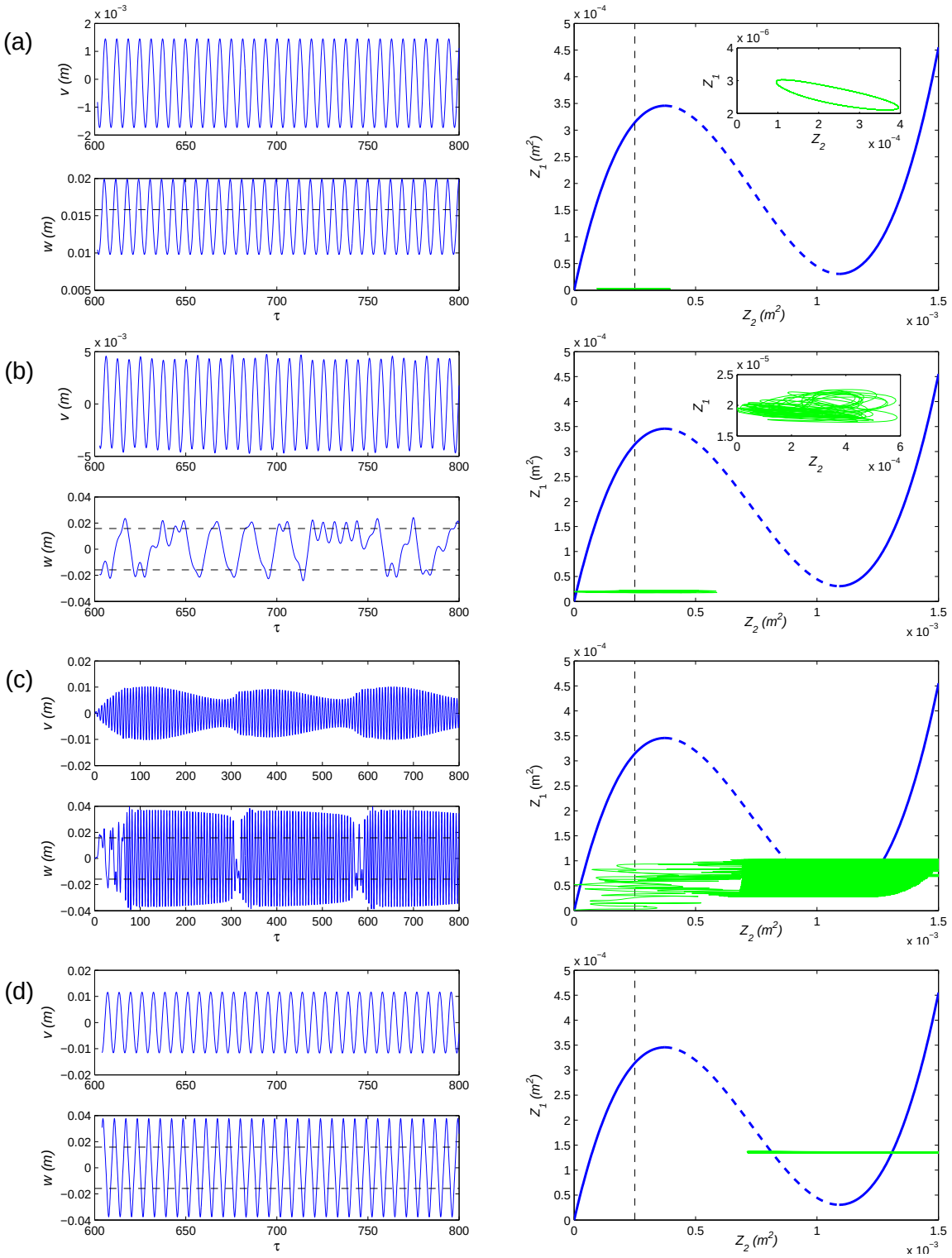

Fig. 5 Time-displacement response of LO and bistable NES, and the motion of the system projected into SIM (a) intra-well oscillation with $G = 0.06\ mm$ (b) chaotic inter-well oscillation with $G = 0.1\ mm$ (c) strongly modulated response with $G = 0.42\ mm$ (d) stable periodic response with $G = 0.55\ mm$

$$\begin{cases} f_1 = -54\,K^2{N_2}^4\sigma - 27\,K^2{N_2}^4 - 96\,K{N_2}^2\delta\,\sigma \\ \quad -24\,K{N_2}^2\lambda_1\,\lambda_2 + 36\,FKN_2\sin\theta_2 - 48\,K{N_2}^2\delta \\ \quad +96\,\sigma\,K{N_2}^2 + 12\,K{N_2}^2 - 32\,\delta^2\sigma - 32\,{\lambda_2}^2\sigma \\ \quad -16\,\delta^2 + 64\,\sigma\,\delta - 16\,{\lambda_2}^2 + 16\,\delta - 32\,\sigma \\ \quad +\frac{1}{N_2}(16\,F\delta\sin\theta_2 + 16\,F\cos\theta_2\lambda_2 - 16\,F\sin\theta_2) \\ f_2 = -9\,K^2{N_2}^5\lambda_1 - 24\,K{N_2}^3\delta\,\lambda_1 + 24\,\lambda_1\,K{N_2}^3 \\ \quad -12\,FK{N_2}^2\cos\theta_2 - 16\,N_2\delta^2\lambda_1 - 16\,N_2\lambda_1\,{\lambda_2}^2 \\ \quad +16\,F\sin\theta_2\lambda_2 - 16\,F\delta\cos\theta_2 + 32\,\lambda_1\,\delta\,N_2 \\ \quad +16F\,\cos\theta_2 - 16\,\lambda_1\,N_2 - 16\,N_2\lambda_2 \\ g = 54\,K^2{N_2}^4 + 96\,K{N_2}^2\delta - 96\,K{N_2}^2 \\ \quad +32\,{\lambda_2}^2 + 32(\delta-1)^2 \end{cases} \tag{19}$$

In [27], it is shown that Eq. (18) has two kinds of fixed point. The first is referred to as an ordinary fixed point. It is located at the branch of SIM and satisfies the condition $f_1 = f_2 = 0$ and $g \neq 0$. The others correspond to the folded singularities. In this case the derivative of Eq. (14) is related to the third equation of Eqs. (19), so it can be found that $g = 0$. Based on this, the system $f_1 = f_2 = 0$ will be discussed and is rewritten in the following matrix form:

$$\begin{bmatrix} \alpha_1 & \alpha_2 \\ \beta_1 & \beta_2 \end{bmatrix} \begin{bmatrix} \sin\theta_2 \\ \cos\theta_2 \end{bmatrix} = \begin{bmatrix} \eta_1 \\ \eta_2 \end{bmatrix} \tag{20}$$

where

$$\begin{cases} \alpha_1 = \frac{1}{N_2}(36FKN_2^2 - 16F + 16F\delta), \quad \alpha_2 = \frac{16F\lambda_2}{N_2} \\ \beta_1 = 16\lambda_2 F, \quad \beta_2 = -12FKN_2^2 + 16F - 16F\delta \\ \eta_1 = 54\,K^2{N_2}^4\sigma + 27\,K^2{N_2}^4 + 96\,K{N_2}^2\delta\,\sigma \\ \quad +24\,K{N_2}^2\lambda_1\,\lambda_2 + 48\,K{N_2}^2\delta - 96\,\sigma\,K{N_2}^2 \\ \quad -12\,K{N_2}^2 + 32\,\delta^2\sigma + 32\,{\lambda_2}^2\sigma + 16\,\delta^2 \\ \quad -64\,\sigma\,\delta + 16\,{\lambda_2}^2 - 16\,\delta + 32\,\sigma \\ \eta_2 = 9\,K^2{N_2}^5\lambda_1 + 24\,K{N_2}^3\delta\,\lambda_1 - 24\,\lambda_1\,K{N_2}^3 \\ \quad +16\,N_2\delta^2\lambda_1 + 16\,N_2\lambda_1\,{\lambda_2}^2 - 32\,\lambda_1\,\delta\,N_2 \\ \quad +16\,\lambda_1\,N_2 + 16\,N_2\lambda_2 \end{cases} \tag{21}$$

By solving Eq. (20), the phase angle of ordinary points θ_2 can be obtained as the determinant does not vanish. For the folded singularities Z_ic, it is observed that $det(A) = 8F^2g/N = 0$, which means that, when $f_2 = 0$ is eliminated, the condition $f_1 = 0$ can be automatically satisfied by Eq. (20). Thus we can study the expression of f_2 only:

$$\sqrt{\beta_1^2 + \beta_2^2}\cos(\theta_2 - \gamma) = \eta_2, \quad \gamma = \arctan(\frac{\beta_1}{\beta_2}) \tag{22}$$

Then θ_2 can be deduced as:

$$\theta_2 = \arctan(\frac{\beta_1}{\beta_2}) + \arccos(\frac{\eta_2}{\sqrt{\beta_1^2+\beta_2^2}}) \tag{23}$$

Based on this, the critical condition of the excitation amplitude for the existence of the folded singularities is:

$$|\frac{\eta_2}{\sqrt{\beta_1^2+\beta_2^2}}| = 1 \tag{24}$$

Thus the threshold of SMR is calculated as:

$$G_{ic} = \epsilon\frac{N_{2i}}{4}\frac{F_1}{F_2} \tag{25}$$

where

$$F_1 = 9\,K^2{N_{2i}}^4\lambda_1 + 24\,K{N_{2i}}^2\delta\,\lambda_1 - 24\,K{N_{2i}}^2\lambda_1 \\ +16\,\delta^2\lambda_1 + 16\,\lambda_1\,{\lambda_2}^2 - 32\,\delta\,\lambda_1 + 16\,\lambda_1 + 16\,\lambda_2 \tag{26}$$

$$F_2 = (9\,K^2{N_{2i}}^4 + 24\,K{N_{2i}}^2\delta - 24\,K{N_{2i}}^2 \\ +16\,{\lambda_2}^2 + 16(\,\delta^2 - 1)^2)^{\frac{1}{2}} \tag{27}$$

3.2 Melnikov analysis for low energy level

The criterion of excitation amplitude to produce SMR at high level of energy having been detected, the next objective is to predict the ignition area of chaotic response at low level of energy. For this, Melnikov analysis is introduced. It is a function that can measure the distance between the stable and unstable manifolds for a saddle of the perturbed system [40,41]. The dynamical system is written as:

$$\dot{z} = f(z) + \epsilon g(z,t); \quad z = \begin{Bmatrix} u_1 \\ u_2 \end{Bmatrix} \in \mathbb{R}^2 \tag{28}$$

where $f(z)$ is a Hamiltonian vector field on $\mathbb{R}^2$ and $\epsilon g(z,t)$ is a small perturbation which does not need to be Hamiltonian itself. To fit this function, the second equation of the system of equations (3) is equivalent to:

$$\ddot{w} + \lambda_2\dot{w} + Kw^3 + \delta w = \ddot{x} \tag{29}$$

Then we define that

$$\begin{cases} \lambda_2 = \epsilon\hat{\lambda_2} \\ \ddot{x} = \epsilon\hat{x} \end{cases} \tag{30}$$

Substituting Eq. (30) into Eq. (29) and transferring it into the form of Eq. (28), the expression can be written as:

$$\begin{cases} \dot{u}_1 = u_2 \\ \dot{u}_2 = -\delta u_1 - K u_1^3 + \epsilon(\hat{x} - \hat{\lambda}_2 u_2) \end{cases} \tag{31}$$

For $\epsilon = 0$, Eq. (31) has two centres at $(u_1, u_2) = (\pm\sqrt{(-\delta/K)}, 0)$ and a hyperbolic saddle at$(u_1, u_2) = (0, 0)$, the Hamiltonian of the system is:

$$H(u_1, u_2) = \frac{u_2^2}{2} + \delta\frac{u_1^2}{2} + K\frac{u_1^4}{4} \tag{32}$$

where the potential function can be written as:

$$U(u_1) = \delta\frac{u_1^2}{2} + K\frac{u_1^4}{4} \tag{33}$$

The corresponding curve is presented in Fig. 6(a). It shows that, when the energy has the local maximum at $u_1 = 0$, a global homoclinic bifurcation will be produced, which implies a transition from intra-well oscillation to inter-well oscillation. The unperturbed homoclinic orbits that connect the saddle point of the potential energy curve are given by:

$$\begin{cases} q_+^0(\tau) = (R \cdot \mathrm{sech}(S\tau), -RS \cdot \mathrm{sech}(S\tau)\ \tanh(S\tau)) \\ q_-^0(\tau) = -q_+^0(\tau) \end{cases} \tag{34}$$

where $S = \pm\sqrt{-\delta}$ and $R = \sqrt{-2\delta/K}$. Additionally, two homoclinic orbits based at $q_\pm^0 = (\pm R, 0)$ are presented in Fig. 6(b). Its function as the pseudo-separatrix for the occurance of chaotic motion will be discussed later.

According to the Melnikov function, the distance between stable and unstable manifolds is given by $M(\tau_0)$:

$$M(\tau_0) = \int_{-\infty}^{\infty} f(q^0(\tau)) \wedge g(q^0(\tau), \tau + \tau_0) d\tau \tag{35}$$

The $\wedge$ operator is the wedge product of $f(q^0(\tau))$ and $g(q^0(\tau), \tau + \tau_0)$. To present the computation of $M(\tau_0)$ for $q_+^0(\tau)$, f and g are written as:

$$f(q^0(\tau)) = \begin{pmatrix} -RS \cdot \mathrm{sech}(S\tau)\tanh(S\tau) \\ -\delta R \cdot \mathrm{sech}(S\tau) - KR^3 \cdot \mathrm{sech}^3(\tau) \end{pmatrix} \tag{36}$$

$$g(q^0(\tau, \tau + \tau_0)) = \begin{pmatrix} 0 \\ \hat{x} - \hat{\lambda}_2 RS \cdot \mathrm{sech}(S\tau)\tanh(S\tau) \end{pmatrix} \tag{37}$$

Thus,

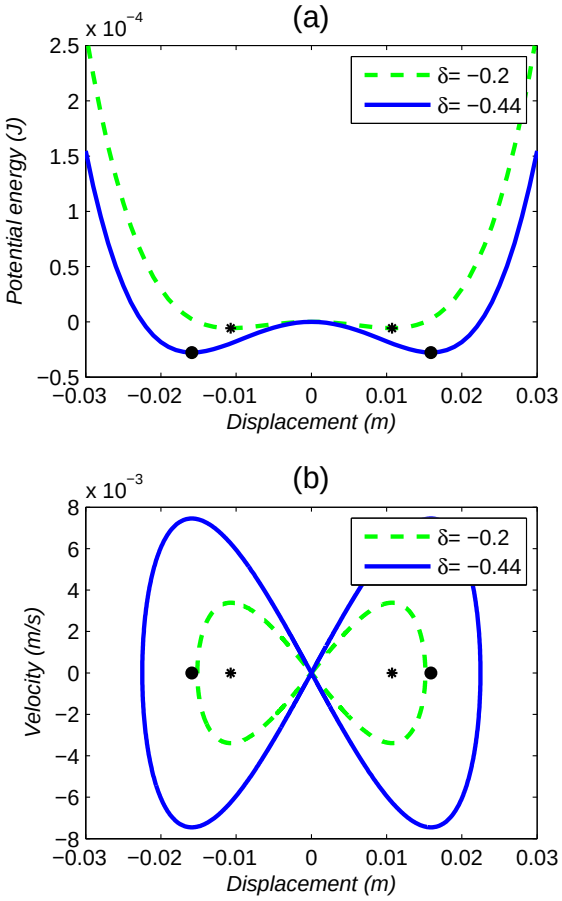

Fig. 6 (a) Potential energy and (b) Hamilton phase plane: pseudo-separatrix

$$M(\tau_0) = -RS\int_{-\infty}^{\infty} \mathrm{sech}(S\tau)\tanh(S\tau)\hat{x}(\tau + \tau_0)d\tau - R^2 S\hat{\lambda}_2 \underbrace{\int_{-\infty}^{\infty} S \cdot \mathrm{sech}^2(S\tau)\tanh^2(S\tau)d\tau}_{=[\frac{\tanh^2}{3}]_{-\infty}^{+\infty}=2/3} \tag{38}$$

Yielding

$$M(\tau_0) = -RS\int_{-\infty}^{\infty} \mathrm{sech}(S\tau)\tanh(S\tau)\hat{x}(\tau + \tau_0)d\tau - \frac{2R^2 S\hat{\lambda}_2}{3} \tag{39}$$

As the energy of excitation decreases, the response of the NES will change from aperiodic alternating cross-well and intra-well oscillation to intra-well oscillation. During this process, the phase trajectory will pass the

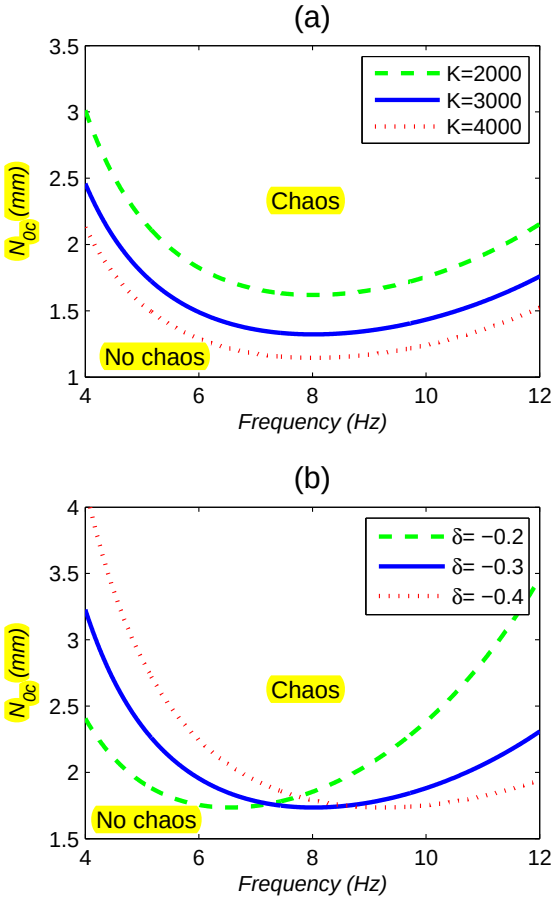

Fig. 7 The critical amplitude for the appearance of intra-well and chaotic oscillations as a function of the excitation frequency, with the various values of (a) cubic stiffness and (b) negative stiffness.

pseudo-separatrix, the amplitude of LO will tend to be stable, and pass through the critical maximum value N_0c. To obtain this value, we suppose that the periodic response of $\hat{x}$ is written as:

$$\hat{x} = \hat{A}cos(\Omega\tau + \phi) \tag{40}$$

Substituting Eq. (40) into Eq. (39), and using the theorem that trigonometric functions are even or odd since $\cos(\Omega(\tau+\tau_0)+\phi) = \cos(\Omega\tau_0+\phi)\cos(\Omega\tau) - \sin(\Omega\tau_0+\phi)\sin(\Omega\tau)$, $M(\tau_0)$ can be expressed as:

$$M(\tau_0) = -\int_{-\infty}^{\infty} \mathrm{sech}(S\tau)\tanh(S\tau)\sin(\frac{\Omega}{S}S\tau)dS\tau \times R\hat{A}\sin(\Omega\tau_0+\phi) - \frac{2R^2S\hat{\lambda}_2}{3} \tag{41}$$

With the method of residues, the integral term can be calculated as:

$$M(\tau_0) = -R\hat{A}\frac{\pi\Omega}{S}\sin(\Omega\tau_0+\phi)\mathrm{sech}(\frac{\pi\Omega}{2S}) - \frac{2R^2S\hat{\lambda}_2}{3} \tag{42}$$

According to Eq. (30), $\hat{A} = -N_1\Omega^2/\epsilon$. By substituting this equation to Eq. (42), $M(\tau_0)$ finally becomes:

$$M(\tau_0) = \sqrt{\frac{2}{K}}\frac{N_1\pi\Omega^3}{\epsilon}\sin(\Omega\tau_0+\phi)\mathrm{sech}(\frac{\pi\Omega}{2\sqrt{-\delta}}) \pm \frac{4\delta\sqrt{-\delta}}{3K}\frac{\lambda_2}{\epsilon} \tag{43}$$

From Melnikov theory, the fact that $M(\tau_0)$ has a zero solution means that the transverse interaction between stable and unstable manifolds exists in the system, which leads to the appearance of chaos. Then we can obtain the necessary condition for this chaos interaction as:

$$N_{0c} = \frac{2\sqrt{2}(-\delta)^{\frac{3}{2}}\cosh(\frac{\pi\Omega}{2\sqrt{-\delta}})}{3\sqrt{K}\pi\Omega^3}\lambda_2 \tag{44}$$

When $N_1 < N_0c$, the movement of the NES will enter one of the two wells. When the excitation exceeds this value, inter-well motion will occur as a consequence of the homoclinic bifurcation. So there is an analytical border that indicates whether the response is likely to chaos or not.

The effects of negative stiffness δ and cubic stiffness K on the Melnikov threshold for homoclinic bifurcation are illustrated in Fig. 7, where the excitation frequency is given by $f = \omega/2\pi$. The curves shown represent a boundary with the upper domain indicating the area for corresponding chaotic inter-well oscillation. From the perspective of the LO amplitude in Fig. 7(a), we can find that increasing the value of cubic stiffness will result in a decreased amplitude threshold for homoclinic bifurcation. In Fig. 7(b), an increase in the negative stiffness δ leads to a shift of the stationary point ($\partial N_{0c}/\partial f = 0$) toward a higher frequency, which means that, if a system has resonance in the high frequency range, using higher negative stiffness is an easier way to obtain a low amplitude threshold.

4 Dynamical efficiency and design criterion

4.1 Efficiency of bistable NES and cubic NES

Since the thresholds have been deduced for each level of energy, the corresponding dynamical efficiency will

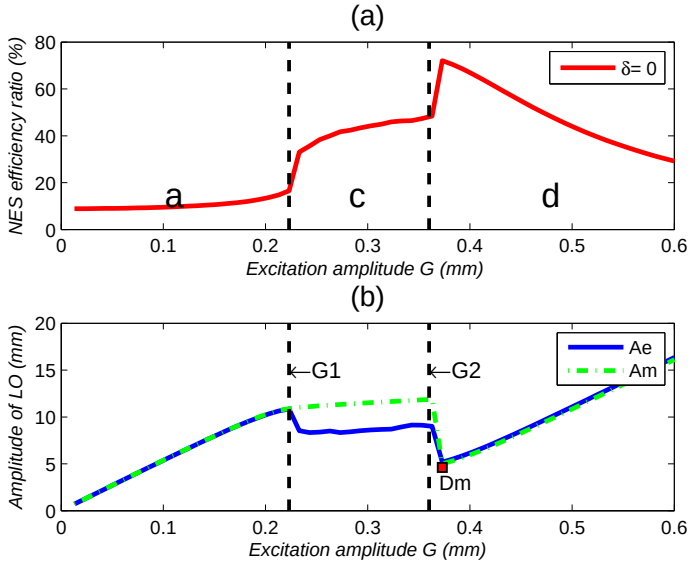

Fig. 8 Efficiency of cubic NES (a) energy dissipation ratio of NES and (b) amplitude of the LO. Ae represents the mean amplitude, and Am the maximum amplitude

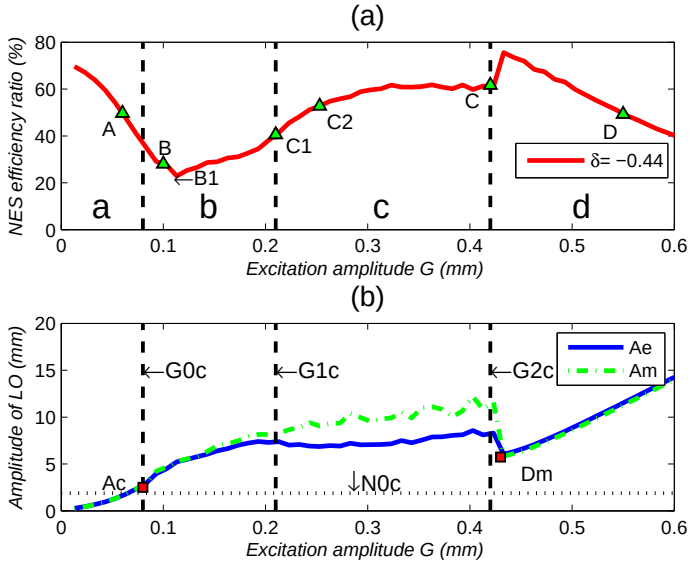

Fig. 9 Efficiency of bistable NES (a) energy dissipation ratio of NES and (b) amplitude of the LO. Ae represents the mean amplitude, and Am the maximum amplitude

be discussed in this section. For a better understanding of the performance of a bistable NES, Fig. 8 and Fig. 9 provide a comparison between a cubic NES and a bistable NES for the energy dissipation ratio and the amplitude of the LO. The energy dissipated by the LO and the NES in the time interval (τ_0, τ) is:

$$\begin{cases} E_{\mathrm{LO}}(\tau) = \int_{\tau_0}^{\tau} \epsilon\lambda_1 \dot{x}^2 d\tau \\ E_{\mathrm{NES}}(\tau) = \int_{\tau_0}^{\tau} \epsilon\lambda_2 (\dot{x} - \dot{y})^2 d\tau \end{cases} \tag{45}$$

Therefore, the energy dissipation ratio of the NES (i.e. the efficiency) can be defined as:

$$r_{\mathrm{NES}} = \frac{E_{\mathrm{NES}}}{E_{\mathrm{LO}} + E_{\mathrm{NES}}} \times 100\% \tag{46}$$

For the cubic NES in Fig. 8, the areas a, c and d respectively represent the fixed point, SMR and fixed point in the SIM structure. Where A_e is the mean amplitude (i.e. average value of the slowly varying en-

velopes), A_m is the maximum amplitude (i.e. maximum value of the slowly varying envelopes). When the input energy is too low to activate the energy pumping of the cubic NES, the efficiency is poor, and the amplitude of LO increases linearly with the excitation amplitude. As the input increases to the range $[G_1, G_2]$, the difference between the mean amplitude and the maximum amplitude is distinguished for SMR, in which the amplitude of NES is no longer stable. When the excitation amplitude passes the threshold G_2 and makes the NES work in area d, an optimal point D_m is observed where Ae and Am are the same at the minimum value, and the efficiency ratio of the NES is maximum, almost 74% of the targeted energy is dissipated by the cubic NES.

For bistable NES in Fig. 9, the areas a, b, c and d represent four different regimes: intra-well oscillation, chaotic inter-well oscillation, SMR and stable periodic response, respectively, where the points A, B, C and D correspond to the excitations $G = 0.06\ mm$, $G = 0.1\ mm$, $G = 0.42\ mm$ and $G = 0.55\ mm$ that we observed previously. Unlike the cubic NES, as the input energy is low, the bistable NES shows high efficiency, even it works in the intra-well oscillation area with small displacement, it can produce a higher dynamical performance. For relatively higher levels of excitation in area b, this regime of chaotic response is observed to have low efficiency of energy dissipation. Comparing the excitation threshold of SMR to that of the cubic NES, as given in Tab. 2, shows that the amplitude band $[G_1c, G_2c]$ is broader once the contribution of negative stiffness is added. Moreover, owing to the higher speed and larger stroke swept in the dynamic transition of negative stiffness area, the efficiency of the bistable NES will be higher than that of the cubic NES. An interesting point is that the threshold of G_1c is close to the corresponding value G_1 of cubic NES. A further study of the theoretical aspects may be useful here. For area d, there is a minimum amplitude D_m, where the LO amplitude starts to increase and the efficiency of NES decreases with the growth of excitation amplitude. By comparing the threshold of $G_2c = 0.42\ mm$ to the calculation result of Eq. (25) that equals $0.422\ mm$, it can be demonstrated that these two solutions correspond with each other well. So in the following section, the analytical solution of G_2c can be used to predict the location of D_m.

Here, it is important to emphasize that at the condition of monochromatic external excitation ($\omega/\omega_0 \approx 1$), the TMD performs better than the cubic NES or bistable NES. The configuration of the primary system coupled either to the TMD or the NES can be obtained by setting k_2 to zero or non-zero value in Eqs. (1), respectively. The main expected advantage of the NES were observed when it was applied to linear multi-dof systems (with remote frequencies), as demonstrated in [42]. Owing to its self-tuning property, energy pumping may be excited in the vicinity of each natural frequency (under periodic excitation), thus providing a substantial reduction of energy for the main structure as compared to the TMD case (which may be tuned to a single frequency only). Additionally, the NES can be effective over a much broader range of frequencies than the TMD and does not suffer from the problem of amplification just outside the target bandwidth [5], thus making it preferable for various engineering applications when the primary system is subject to harmonic forcing in a wide range of excitation frequencies.

Table 2 Excitation threshold

bistable NES (mm)			
G_1c	0.21	G_2c	0.42
G_0c	0.08		
cubic NES (mm)			
G_1	0.22	G_2	0.36

4.2 Detailed analysis of each regime

To further explain the efficiency and verify the thresholds proposed in previous methods, the pseudo-separatrix mentioned above, the Hilbert transform and wavelet transform are introduced to discuss the detailed dynamics in the following subsection.

4.2.1 Intra-well oscillation

In Fig. 9, the threshold G_0c exists between areas a and b, when the LO excited at this value, the corresponding oscillation amplitude A_c obtained is close to the dashed line N_0c calculated by Eq. (44), so it proves that the numerical result coincides with the analytical prediction. When the energy is lower than G_0c, as shown in Fig. 10(b), the cyclic projection in the SIM structure is under the dashed line N_0c, which corresponds to Fig. 10(d) where the phase trajectory is inner the pseudo-separatrix. The red curve in Fig. 10(c) shows that the bistable NES works around the stable equilibrium on the force-displacement curve. Due to the asymmetricity of the force-displacement curve, the two sides of the amplitude of NES presented in Fig. 10(a) are also asymmetric. Since the initial nonlinear stiffness around the stable equilibrium is far larger than that of cubic NES, which is close to zero, the bistable NES can produce nonlinear beating even under a small excitation.

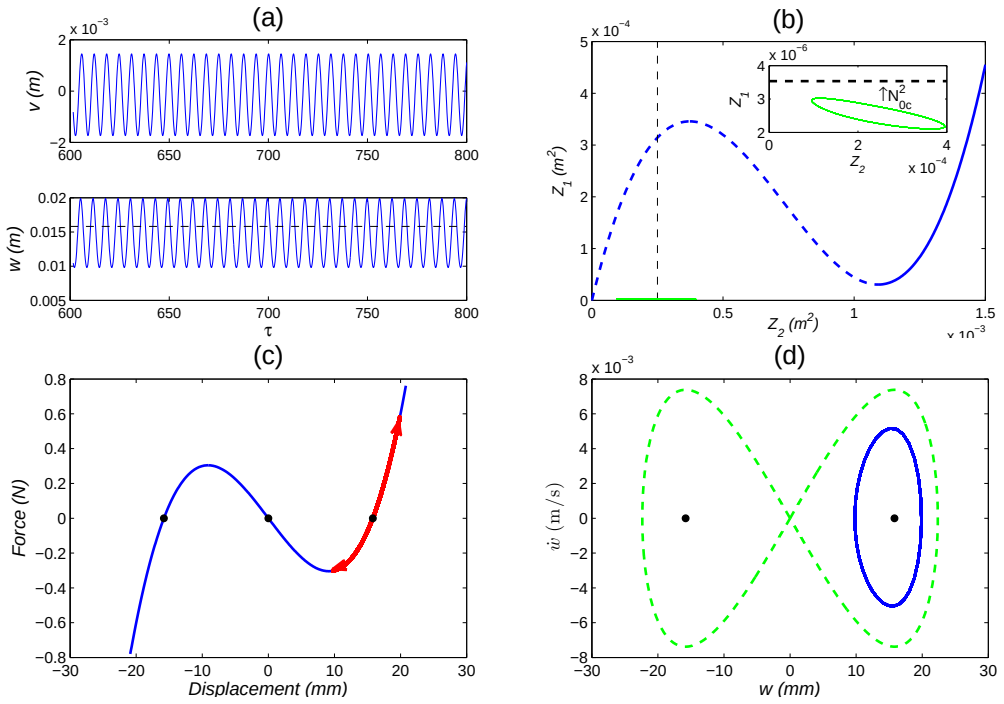

Fig. 10 Response corresponding to point A (a) time-displacement response (b) projection in SIM structure (c) working range in the force-displacement relation (d) phase trajectory of NES

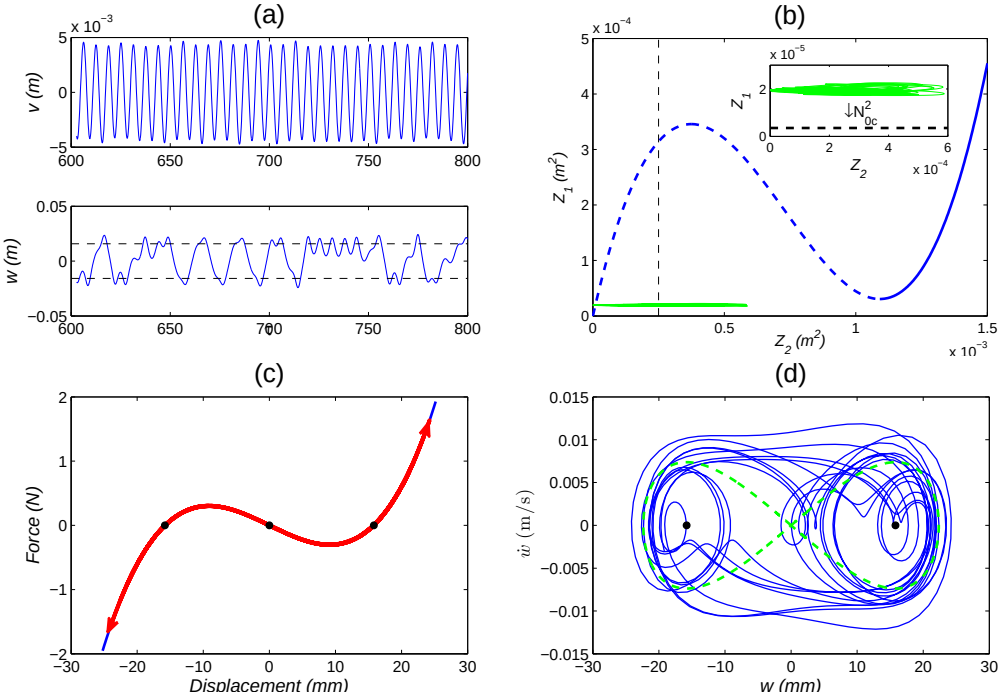

Fig. 11 Response corresponding to point B (a) time-displacement response (b) projection in SIM structure (c) working range in the force-displacement relation (d) phase trajectory of NES

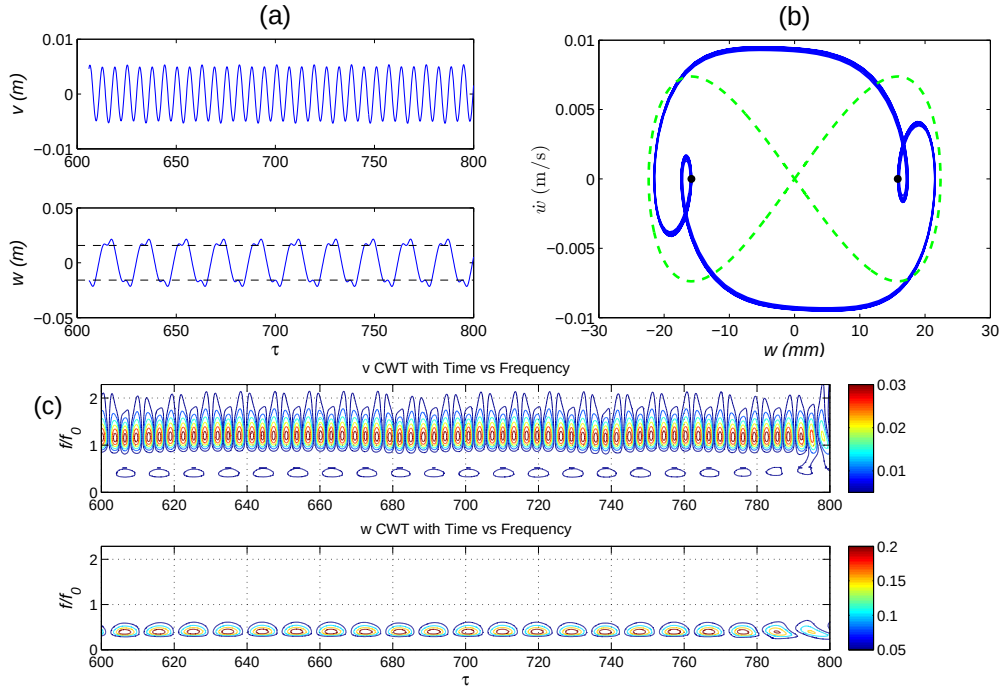

Fig. 12 Response corresponding to point B_1 (a) time-displacement response (b) phase trajectory of NES (c) wavelet transform: 1:3 subharmonic resonance. Where the natural frequency of LO (f_0) is given by $f_0 = 2\pi/\omega_0$.

Therefore, the bistable NES can have a high efficiency ratio with low energy input.

4.2.2 Chaotic inter-well oscillation

As the excitation amplitude increases to the range of response *b*, the working force-displacement range of the NES becomes large and starts to pass the two stable equilibria. It is observed that the dynamic trajectory escapes from one potential well to the other, achieving a global snap-through motion. The chaotic behaviour in this regime is identified in [37], where the Lyapunov characteristic exponents are calculated and the values of exponents are found to be positive. In Fig. 11(b), the chaotic projection in the SIM structure is above the dashed line N_0c, which means that enough energy is supplied so to overcome the potential barrier: the hill-top of Fig. 4. With reference of the pseudo-separatrix, the outer, inner and crossing transient trajectories on the phase diagram are observed consecutively in Fig. 11 (d). These three regimes correspond respectively to the steady transition motion between two stable equilibria, the transition motion captured by a stable equilibrium and the subharmonic nonlinear beating.

In Fig. 9 it is interesting to note the existence of a particular response at point B_1, where the energy dissipation ratio is the lowest. Fig. 12 shows the corresponding time-displacement response and the phase trajectory. It can been seen that this response is no longer chaotic and shows periodic performance. By introducing the wavelet transform method, the frequency components of the LO and bistable NES are obtained, which illustrates that the transition point represents a resonance capture with the frequency of 1:3 subharmonic. With the increase of input energy, the periodic performance will disappear while the component of 1:3 subharmonic response will hold for the following response.

4.2.3 Strongly modulated response

To illustrate the global performance of the SMR, three specified responses with the excitation amplitude of 0.21 *mm*, 0.25 *mm* and 0.42 *mm* are calculated and presented in Fig. 13, where the first and the last corresponding points are located at the two thresholds of SMR. In these responses, three different TET mechanisms of bistable NES are observed and classified as:

1. Fundamental TET (1:1 resonance capture);
2. Subharmonic resonance capture TET;
3. TET initiated by nonlinear beating.

The first column of Fig. 13 shows the time displacement response of the LO and bistable NES, the second column shows the corresponding instantaneous am-

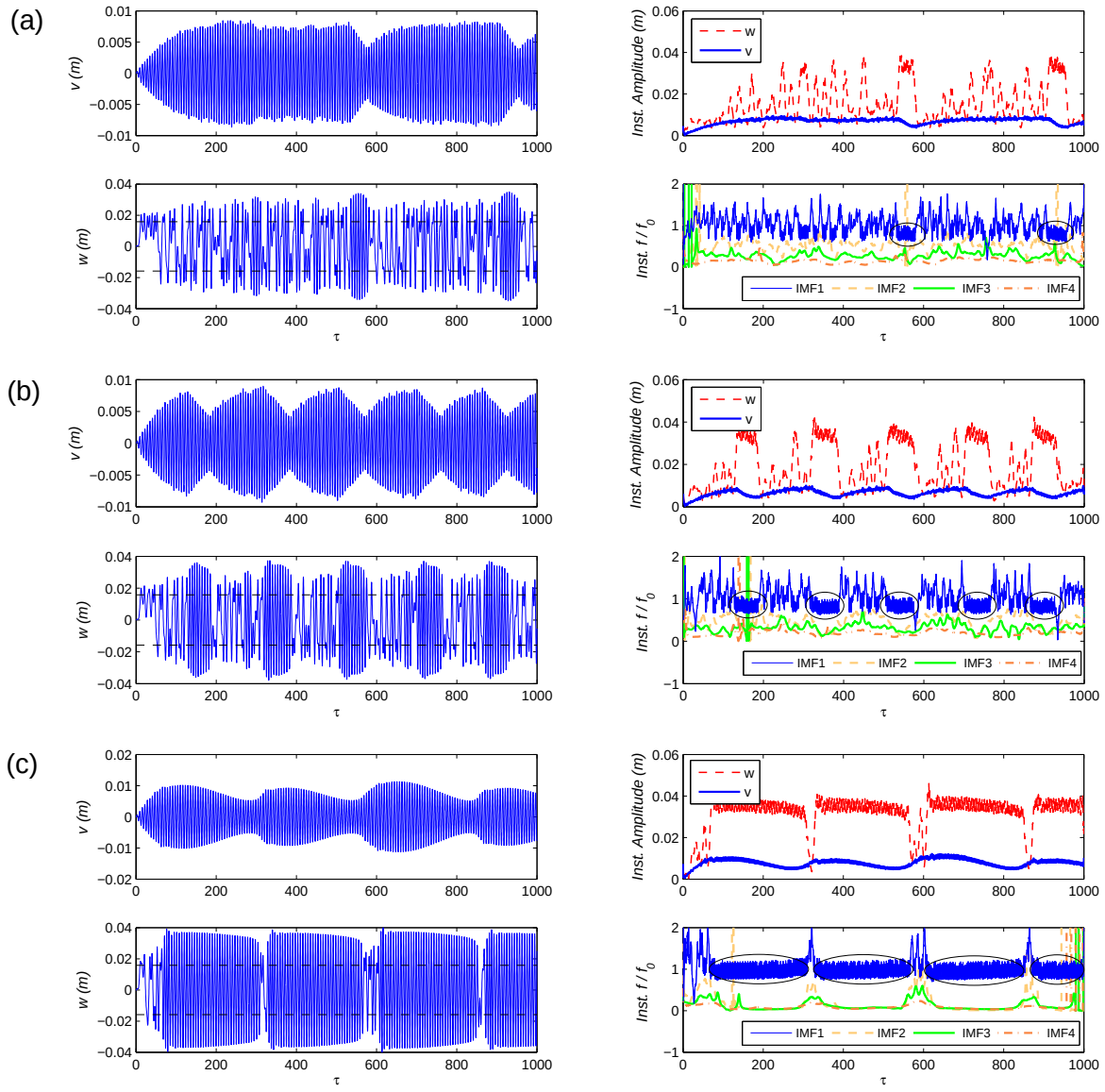

Fig. 13 SMR response in the first column, and the corresponding instantaneous amplitude and frequency in the second column, for different types of energy: (a) input $G = 0.21\ mm$, corresponding to point C_1; (b) input $G = 0.25\ mm$, corresponding to point C_2; (c) input $G = 0.42\ mm$, corresponding to point C. Where the instantaneous amplitude of w is inferred from the leading (first) IMF, the instantaneous frequency of bistable NES is defined as f, and the natural frequency of LO is defined as f_0.

plitude and frequency. To illustrate the basic underlying dynamic mechanism of bistable NES, the empirical mode decomposition (EMD) applied to decomposition of nonlinear and nonstationary signals is adopted [43]. With this method, a collection of intrinsic mode functions (IMFs) is obtained. Then Hilbert Transform is used to calculate the instantaneous frequency and amplitude. Fig. 14 illustrates the frequency components of the LO and bistable NES with the wavelet transform method. By combing these two figures, it can be found that: as the instantaneous frequency of leading (first) IMF of the bitable NES is concentrated on the natural frequency of the LO (i.e. the area of ellipses), the fundamental TET takes place and the dynamics is captured in the domain of attraction of 1:1 resonant manifold. This area is additionally demonstrated by the red zone of bistable NES in Fig. 14. It is also represented the in phase NNM manifold $S11+$ in the Frequency Energy Plot (FEP) [44]. At this regime, large targeted energy is extracted and dissipated by bistable NES, leading to a fast decrease of the LO amplitude.

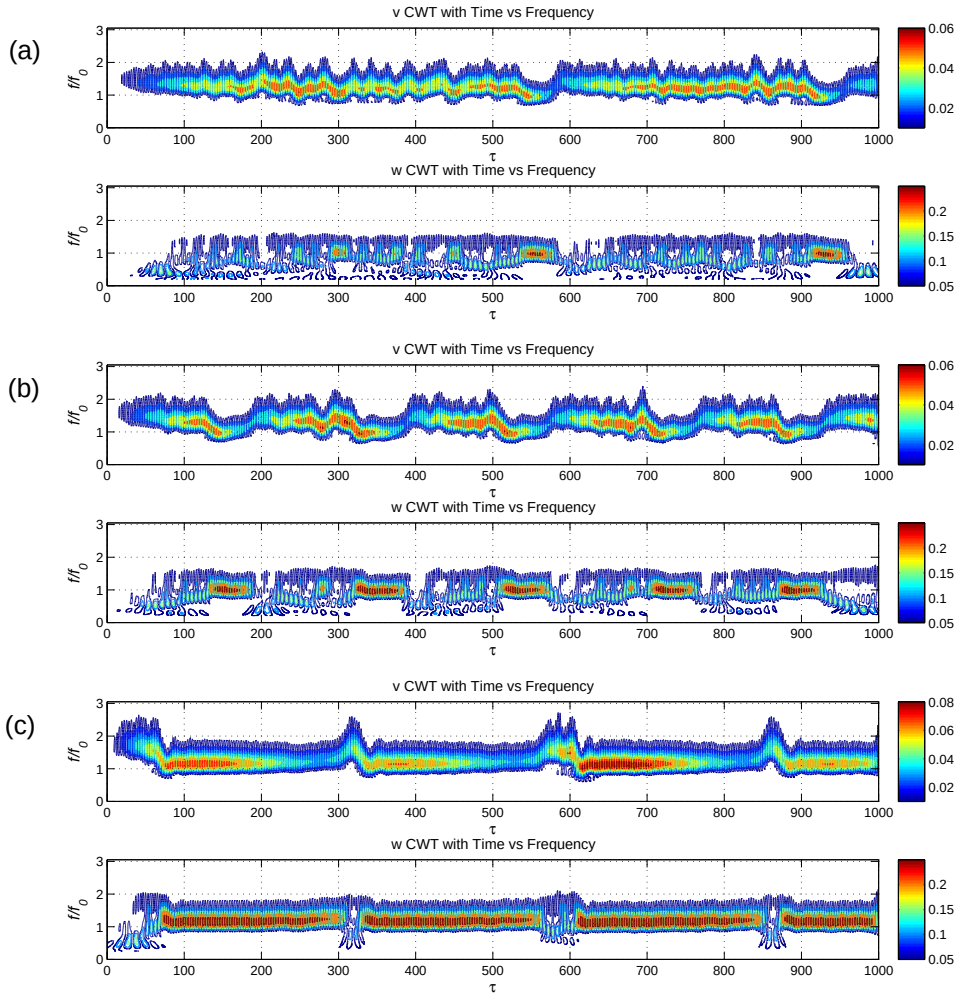

Fig. 14 Wavelet transform for different type of energy: (a) input $G = 0.21mm$ corresponding to point C_1; (b) input $G = 0.25mm$ corresponding to point C_2; (c) input $G = 0.42mm$ corresponding to point C

When the LO amplitude decreases to a certain value, the dynamics transfers to the subharmonic resonance capture TET, where the contribution of 1:3 subharmonic resonance response is observed. Owing to its low energy dissipation ratio and the continuous energy input, the LO amplitude starts to increase, and the duration of this transition is small, resulting in a fast resonance escape to the last regime: TET initiated by nonlinear beating. In this regime, three different response components are observed: a) Fundamental nonlinear beating, occurs in the motion that captured by a stable equilibrium, b) Subharmonic nonlinear beating, c) Nonlinear beating that occurs in the steady transition motions between two stable equilibria.

From Fig. 14, it can be found that the contribution of each regime is related to the input of excitation energy. When the input G is 0.21 mm, the interval of fundamental TET is small and the nonlinear beating regime plays a large prolonged part in the process. When $G = 0.25$ mm, the duration of the fundamental TET regime starts to increase with the decrease of TET initiated by nonlinear beating. As the input reaches the maximum of 0.42 mm, the fundamental TET makes the largest contribution to the process while the transition of subharmonic TET and TET initiated by nonlinear beating are decreased to a narrow zone. In this case, the chaotic aspect almost disappears, and the 1:1 resonance is the strongest, making the NES transfer a relatively high amount of energy in a finite time interval.

4.3 Optimal design criterion

As shown in Fig. 9, the optimal working point is located at the lowest value of the second stable branch of the SIM, in which the efficiency reaches its maximal value. In this case, there exist 1:1 resonance between

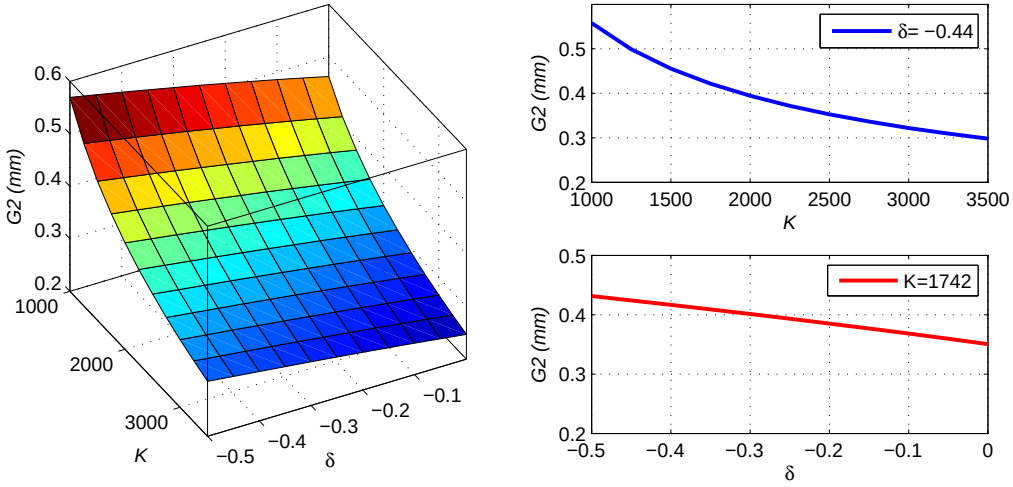

Fig. 15 Controlling the optimal working point of NES by adjusting the nonlinear stiffness K and negative stiffness δ

bistable NES and LO. The comparison of SIM structure between cubic NES and bistable NES can be found in Fig. 2, which shows that, after the addition of the negative stiffness part, the location of optimal point D_m shifts to right, and the corresponding excitation amplitude becomes higher. For this, it is suggested that, if the primary system is excited at a fixed periodic loading, the objective of the optimal design should be to adjust the parameters of NES so as to make it work at the location D_m. By introducing Eq. (25), the excitation amplitude at this point is calculated with the nonlinear stiffness K and negative stiffness δ, as shown in Fig. 15. Here, it can be observed that, adjusting these two variables K and δ is feasible to control the value of G_2c in a certain range, so as to ensure the response of NES located at its optimal point.

For this, a configuration to achieve the negative stiffness and the cubic stiffness is proposed. Where the pure cubic stiffness is obtained by means of two transverse linear springs with no pretension in their vertical direction [5], the essentially negative stiffness component is produced by adopting the method of pre-compressing two springs at initial position [32], so as to achieve the bistable geometry. In this structure, an amount of potential energy is pre-stored and the two stable equilibria are obtained when both springs are in the unstretched state. The corresponding force displacement relationship based on Taylor expansion is given by:

$$f(w) = -2k\frac{l_p}{l_0}w + k\frac{l_p + l_0}{l_0^3}w^3 \tag{47}$$

In this equation, the value of cubic stiffness K is related to the stiffness of spring k and the free length l_0, where the influence of pre-compressed length l_p is so small that it can be neglected. For the negative stiffness δ, it mainly depends on the value of the pre-compressed length l_p since the two springs are installed. As the two springs of a cubic NES are fixed for engineering applications, adjusting the pre-compressed length l_p would provide an alternative way to increase the band in which excitation amplitude is robust. By obtaining the anticipated negative stiffness, the NES can be adjusted to work at the optimal point with its best performance.

5 Conclusion

In this paper, the dynamic response of a 2 DOF system comprising a harmonically excited LO strongly coupled to a bistable NES is investigated. An analytically obtained SIM is used to explain the different response regimes. Unlike cubic NES, bistable NES only follows the second stable branch of the SIM. Asymptotic analysis and Melnikov analysis are respectively used to obtain the thresholds of different response regimes at different energy levels. These analytical solutions are verified in numerical simulation, which correctly predicts the occurrence of intra-well oscillation or chaotic inter-well oscillation, and the transition between SMR and stable periodic response.

The efficiency of different response regimes is studied and demonstrates that a bistable NES working in the first regime with intra-well oscillation can transfer the targeted energy with a relatively high efficiency, but the chaotic inter-well response dissipates energy with low efficiency. For this regime, a point with 1:3 subharmonic resonance captures exists where its effi-

ciency is the lowest. This result is contrary to the traditional idea that 1:3 subharmonic resonance may result in a strong energy exchange and dissipation under periodic excitation. About the band of excitation amplitude with the occurrence of SMR, it becomes broader with the addition of negative stiffness, and the efficiency of bistable NES in this band is larger than that of cubic NES. With the Hilbert transform and wavelet transform, three different TET mechanisms are observed and it shows that 1:1 resonance is mainly responsible for the efficient TET.

Finally, an optimal point located at the boundary between the SMR and stable periodic response is found, at which the efficiency of NES is largest and the amplitude of LO is smallest. Based on this, an optimal design criterion and the corresponding configuration are proposed. By adjusting the pre-compressed length of spring, bistable NES can be designed to robustly work at its best performance for a range of excitation.

References

1. Vakakis, A.F., Gendelman, O.V., Bergman, L.A., McFarland, D.M., Kerschen, G., Lee, Y.S.: Targeted Energy Transfer in Mechanical and Structural Systems, vol. 156. Springer Science & Business Media, Berlin (2008)
2. Lee, Y., Vakakis, A.F., Bergman, L., McFarland, D., Kerschen, G., Nucera, F., Tsakirtzis, S., Panagopoulos, P.: Passive non-linear targeted energy transfer and its applications to vibration absorption: a review. Proc. Inst. Mech. Eng. Part K J. Multibody Dyn **222**(2), 77–134 (2008)
3. Gendelman, O.V., Manevitch, L.I., Vakakis, A.F., Mcloskey, R.: Energy pumping in nonlinear mechanical oscillators: part i: dynamics of the underlying hamiltonian systems. J. Appl. Mech. **68**(1), 34–41 (2001)
4. Vakakis, A.F., Gendelman, O.V.: Energy pumping in nonlinear mechanical oscillators: part ii: resonance capture. J. Appl. Mech. **68**(1), 42–48 (2001)
5. Gourdon, E., Alexander, N.A., Taylor, C.A., Lamarque, C.H., Pernot, S.: Nonlinear energy pumping under transient forcing with strongly nonlinear coupling: Theoretical and experimental results. J. Sound Vib. **300**(3), 522–551 (2007)
6. Lee, Y.S., Kerschen, G., McFarland, D.M., Hill, W.J., Nichkawde, C., Strganac, T.W., Bergman, L.A., Vakakis, A.F.: Suppressing aeroelastic instability using broadband passive targeted energy transfers, part 2: experiments. AIAA journal **45**(10), 2391–2400 (2007)
7. Viguié, R., Kerschen, G., Golinval, J.C., McFarland, D., Bergman, L., Vakakis, A., Van de Wouw, N.: Using passive nonlinear targeted energy transfer to stabilize drillstring systems. Mechanical Systems and Signal Processing **23**(1), 148–169 (2009)
8. Gourc, E., Seguy, S., Michon, G., Berlioz, A., Mann, B.: Quenching chatter instability in turning process with a vibro-impact nonlinear energy sink. J. Sound Vib. **355**, 392–406 (2015)
9. Nucera, F., Iacono, F.L., McFarland, D., Bergman, L., Vakakis, A.: Application of broadband nonlinear targeted energy transfers for seismic mitigation of a shear frame: Experimental results. J. Sound Vib. **313**(1), 57–76 (2008)
10. Luo, J., Wierschem, N.E., Hubbard, S.A., Fahnestock, L.A., Quinn, D.D., McFarland, D.M., Spencer, B.F., Vakakis, A.F., Bergman, L.A.: Large-scale experimental evaluation and numerical simulation of a system of nonlinear energy sinks for seismic mitigation. Eng. Struct. **77**, 34–48 (2014)
11. Anubi, O.M., Crane, C.: A new semiactive variable stiffness suspension system using combined skyhook and nonlinear energy sink-based controllers. IEEE Transactions on Control Systems Technology **23**(3), 937–947 (2015)
12. McFarland, D.M., Bergman, L.A., Vakakis, A.F.: Experimental study of non-linear energy pumping occurring at a single fast frequency. Int. J. Non-Linear Mech. **40**(6), 891–899 (2005)
13. Kerschen, G., McFarland, D.M., Kowtko, J.J., Lee, Y.S., Bergman, L.A., Vakakis, A.F.: Experimental demonstration of transient resonance capture in a system of two coupled oscillators with essential stiffness nonlinearity. J. Sound Vib. **299**(4), 822–838 (2007)
14. Gendelman, O.V., Sigalov, G., Manevitch, L.I., Mane, M., Vakakis, A.F., Bergman, L.A.: Dynamics of an eccentric rotational nonlinear energy sink. J. Appl. Mech. **79**(1), 011,012 (2012)
15. Sigalov, G., Gendelman, O., Al-Shudeifat, M., Manevitch, L., Vakakis, A., Bergman, L.: Resonance captures and targeted energy transfers in an inertially-coupled rotational nonlinear energy sink. Nonlinear Dyn. **69**(4), 1693–1704 (2012)
16. Gendelman, O.V.: Targeted energy transfer in systems with non-polynomial nonlinearity. J. Sound Vib. **315**(3), 732–745 (2008)
17. Lamarque, C.H., Gendelman, O.V., Savadkoohi, A.T., Etcheverria, E.: Targeted energy transfer in mechanical systems by means of non-smooth nonlinear energy sink. Actamechanica **221**(1-2), 175 (2011)
18. Nucera, F., Vakakis, A.F., McFarland, D., Bergman, L., Kerschen, G.: Targeted energy transfers in vibro-impact oscillators for seismic mitigation. Nonlinear Dyn. **50**(3), 651–677 (2007)
19. Al-Shudeifat, M.A., Wierschem, N., Quinn, D.D., Vakakis, A.F., Bergman, L.A., Spencer, B.F.: Numerical and experimental investigation of a highly effective single-sided vibro-impact non-linear energy sink for shock mitigation. Int. J. Non-Linear Mech. **52**, 96–109 (2013)
20. Bellet, R., Cochelin, B., Herzog, P., Mattei, P.O.: Experimental study of targeted energy transfer from an acoustic system to a nonlinear membrane absorber. J. Sound Vib. **329**(14), 2768–2791 (2010)
21. AL-Shudeifat, M.A.: Asymmetric magnet-based nonlinear energy sink. J. Comput. Nonlinear Dynam **10**(1), 014,502 (2015)
22. Gourc, E., Michon, G., Seguy, S., Berlioz, A.: Experimental investigation and design optimization of targeted energy transfer under periodic forcing. J. Vib. Acoust. **136**(2), 021,021 (2014)
23. Li, T., Seguy, S., Berlioz, A.: Optimization mechanism of targeted energy transfer with vibro-impact energy sink under periodic and transient excitation. Nonlinear Dyn. **87**(4), 2415–2433 (2016)
24. Vaurigaud, B., Ture Savadkoohi, A., Lamarque, C.H.: Targeted energy transfer with parallel nonlinear energy sinks. part i: design theory and numerical results. Nonlinear Dyn. **66**(4), 763–780 (2011)
25. Gendelman, O., Alloni, A.: Dynamics of forced system with vibro-impact energy sink. J. Sound Vib. **358**, 301–314 (2015)

26. Gendelman, O., Starosvetsky, Y., Feldman, M.: Attractors of harmonically forced linear oscillator with attached nonlinear energy sink i: Description of response regimes. Nonlinear Dyn. **51**(1), 31–46 (2008)
27. Starosvetsky, Y., Gendelman, O.: Strongly modulated response in forced 2dof oscillatory system with essential mass and potential asymmetry. Physica D: Nonlinear Phenomena **237**(13), 1719–1733 (2008)
28. Johnson, D.R., Thota, M., Semperlotti, F., Wang, K.: On achieving high and adaptable damping via a bistable oscillator. Smart Materials and Structures **22**(11), 115,027 (2013)
29. Gourdon, E., Lamarque, C.H.: Energy pumping with various nonlinear structures: numerical evidences. Nonlinear Dyn. **40**(3), 281–307 (2005)
30. Savadkoohi, A.T., Manevitch, L.I., Lamarque, C.H.: Analysis of the transient behavior in a two dof nonlinear system. Chaos, Solitons & Fractals **44**(6), 450–463 (2011)
31. Harne, R., Thota, M., Wang, K.: Bistable energy harvesting enhancement with an auxiliary linear oscillator. Smart Materials and Structures **22**(12), 125,028 (2013)
32. Mohammad A, A.S.: Highly efficient nonlinear energy sink. Nonlinear Dyn. **76**(4), 1905–1920 (2014)
33. Habib, G., Romeo, F.: The tuned bistable nonlinear energy sink. Nonlinear Dyn. **89**(1), 179–196 (2017)
34. Harne, R., Wang, K.: A review of the recent research on vibration energy harvesting via bistable systems. Smart materials and structures **22**(2), 023,001 (2013)
35. Manevitch, L., Sigalov, G., Romeo, F., Bergman, L., Vakakis, A.: Dynamics of a linear oscillator coupled to a bistable light attachment: analytical study. J. Appl. Mech. **81**(4), 041,011 (2014)
36. Romeo, F., Sigalov, G., Bergman, L.A., Vakakis, A.F.: Dynamics of a linear oscillator coupled to a bistable light attachment: Numerical study. J. Comput. Nonlinear Dynam. **10**(1), 011,007 (2015)
37. Romeo, F., Manevitch, L., Bergman, L., Vakakis, A.: Transient and chaotic low-energy transfers in a system with bistable nonlinearity. Chaos: An Interdisciplinary Journal of Nonlinear Science **25**(5), 053,109 (2015)
38. Fang, X., Wen, J., Yin, J., Yu, D.: Highly efficient continuous bistable nonlinear energy sink composed of a cantilever beam with partial constrained layer damping. Nonlinear Dyn. **87**(4), 2677–2695 (2017)
39. Mattei, P.O., Ponçot, R., Pachebat, M., Côte, R.: Nonlinear targeted energy transfer of two coupled cantilever beams coupled to a bistable light attachment. J. Sound Vib. **373**, 29–51 (2016)
40. Wiggins, S.: Introduction to applied nonlinear dynamical systems and chaos, vol. 2. Springer Science & Business Media (2003)
41. Guckenheimer, J., Holmes, P.J.: Nonlinear oscillations, dynamical systems, and bifurcations of vector fields, vol. 42. Springer Science & Business Media (2013)
42. Starosvetsky, Y., Gendelman, O.: Dynamics of a strongly nonlinear vibration absorber coupled to a harmonically excited two-degree-of-freedom system. J. Sound Vib. **312**(1), 234–256 (2008)
43. Huang, N.E., Shen, Z., Long, S.R., Wu, M.C., Shih, H.H., Zheng, Q., Yen, N.C., Tung, C.C., Liu, H.H.: The empirical mode decomposition and the hilbert spectrum for nonlinear and non-stationary time series analysis. In: Proceedings of the Royal Society of London A, vol. 454, pp. 903–995 (1998)
44. Kerschen, G., Kowtko, J.J., McFarland, D.M., Bergman, L.A., Vakakis, A.F.: Theoretical and experimental study of multimodal targeted energy transfer in a system of coupled oscillators. Nonlinear Dyn. **47**(1), 285–309 (2007)